

A study of convective core overshooting as a function of stellar mass based on two-dimensional hydrodynamical simulations

I. Baraffe,^{1,2★} J. Clarke,¹ A. Morison,¹ D. G. Vlaykov^①,¹ T. Constantino,¹ T. Goffrey,³ T. Guillet^①,¹
A. Le Saux^{1,2} and J. Pratt⁴

¹Physics and Astronomy, University of Exeter, Exeter EX4 4QL, UK

²École Normale Supérieure, Lyon, CRAL (UMR CNRS 5574), Université de Lyon, 69007 Lyon, France

³Centre for Fusion, Space and Astrophysics, Department of Physics, University of Warwick, Coventry CV4 7AL, UK

⁴Lawrence Livermore National Laboratory, 7000 East Ave, Livermore, CA 94550, USA

Accepted 2022 December 23. Received 2022 December 23; in original form 2022 November 8

ABSTRACT

We perform two-dimensional (2D) numerical simulations of core convection for zero-age main-sequence stars covering a mass range from 3 to 20 M_{\odot} . The simulations are performed with the fully compressible time-implicit code MUSIC. We study the efficiency of overshooting, which describes the ballistic process of convective flows crossing a convective boundary, as a function of stellar mass and luminosity. We also study the impact of artificially increasing the stellar luminosity for 3 M_{\odot} models. The simulations cover hundreds to thousands of convective turnover time-scales. Applying the framework of extreme plume events previously developed for convective envelopes, we derive overshooting lengths as a function of stellar masses. We find that the overshooting distance (d_{ov}) scales with the stellar luminosity (L) and the convective core radius (r_{conv}). We derive a scaling law $d_{\text{ov}} \propto L^{1/3} r_{\text{conv}}^{1/2}$, which is implemented in a one-dimensional stellar evolution code and the resulting stellar models are compared to observations. The scaling predicts values for the overshooting distance that significantly increase with stellar mass, in qualitative agreement with observations. Quantitatively, however, the predicted values are underestimated for masses $\gtrsim 10 M_{\odot}$. Our 2D simulations show the formation of a nearly adiabatic layer just above the Schwarzschild boundary of the convective core, as exhibited in recent three-dimensional simulations of convection. The most luminous models show a growth in size with time of the nearly adiabatic layer. This growth seems to slow down as the upper edge of the nearly adiabatic layer gets closer to the maximum overshooting length and as the simulation time exceeds the typical thermal diffusive time-scale in the overshooting layer.

Key words: convection – hydrodynamics – stars: evolution.

1 INTRODUCTION

One of the major uncertainties in stellar evolution models is the treatment of mixing taking place at convective boundaries (see Stancliffe et al. 2016). Convective motions do not abruptly stop at the classical Schwarzschild boundary, but extend beyond it and lead to the process of convective boundary mixing (CBM). The complex dynamics resulting from convective flows penetrating in stable layers drives the transport of chemical species and heat, strongly affecting the structure and the evolution of stars. The same complex dynamics can also drive transport of angular momentum, impacting the rotational evolution of stars, the generation of magnetic field in their interior, and their magnetic activity. CBM affects the evolution of all stars that develop a convective envelope, core, or shell. Its treatment is one of the oldest unsolved problems of stellar structure and evolution theory (Shaviv & Salpeter 1973). This extra mixing could significantly alter the size of a convective core, the lifetime of major burning phases, or the surface chemistry over a wide range of stellar masses. It can impact the entire evolution of massive

stars ($M \gtrsim 8 M_{\odot}$), determining their structure before core-collapse supernova explosion and thus affecting nucleosynthetic yields that are crucial for galactic evolution studies (Arnett & Meakin 2011). There is ample observational evidence pointing towards the need for extra internal mixing to explain a wide range of observations, such as eclipsing binaries (Claret & Torres 2016), colour–magnitude diagrams (Rosenfield et al. 2017), or asteroseismology (Bossini et al. 2015). Rosenfield et al. (2017) illustrate the uncertainty due to the treatment of core overshooting on ages and on morphological changes in stellar evolution tracks, significantly impacting stellar population studies. An increasing number of observational studies also suggests an increase of CBM efficiency with stellar mass, using eclipsing binaries (see Claret & Torres 2019, and references therein) or Hertzsprung–Russell diagrams (HRDs) of massive stars (Castro et al. 2014). In a recent study, Johnston (2021) confirms that current stellar models with no or with little CBM usually underpredict the mass of convective cores. While such comparisons between stellar models and observations cannot identify a mechanism responsible for mixing at the convective boundaries, Johnston (2021) concludes that a range of efficiencies for the mixing mechanism(s) should be used. In addition to CBM, additional mixing could be due to rotation (Zahn 1992) or internal gravity waves (Schatzman 1993). The latter

* E-mail: i.baraffe@ex.ac.uk

are connected to CBM as they are excited at convective boundaries by turbulent convective motions (Press 1981; Goldreich & Kumar 1990; Lecoanet & Quataert 2013) and penetrating flows (Rieutord & Zahn 1995; Montalbán & Schatzman 2000; Pinçon, Belkacem & Goupil 2016).

CBM is a generic term that encompasses different processes, namely *penetration*, *overshooting*, or *entrainment*. The first term describes motions that cross a convective boundary and alter the background in such a way that the location of the convective boundary, defined by the Schwarzschild or the Ledoux criterion, moves inward or outward, resulting in the extension of the convective region. Overshooting usually describes convective penetrative motions that do not alter the background but can still result in more or less efficient mixing (Zahn 1991). In the literature, the terms overshooting and penetration are often used interchangeably. These processes have been described in stellar evolution models by an overshooting distance d_{ov} and/or a diffusion coefficient that remains constant or exponentially decays over the overshooting length (Freytag, Ludwig & Steffen 1996). These parameters are usually calibrated to fit observations. The temperature gradient in the overshooting region is set to either the radiative or the adiabatic temperature gradient (see e.g. Michielsen et al. 2019). The third term *entrainment* is used to characterize shear-induced turbulent motions at the interface between the convectively stable and unstable regions driven by convective penetrative motions (plumes or eddies). Interfacial instabilities contribute to mixing fluids of different compositions and/or densities, eroding the convective boundary. This one can then grow in time following an entrainment rate characterized by the bulk Richardson number (Fernando 1991; Strang & Fernando 2001). Entrainment rates based on hydrodynamical simulations performed in a stellar context (Meakin & Arnett 2007; Jones et al. 2017; Cristini et al. 2019) are also implemented in stellar evolution codes to describe the extension of convective cores and shells (Staritsin 2013; Scott et al. 2021). However, as shown by Scott et al. (2021), adopting entrainment rates derived from existing stellar hydrodynamical simulations to main-sequence stellar models produces unrealistic growth of the convective cores. The parameters that control the entrainment rates need to be decreased by several orders of magnitude to reproduce observations, questioning the reliability of the quantitative rates derived from existing numerical simulations and even the existence of an entrainment process for main-sequence convective cores.

Describing and isolating these different processes characterizing CBM and at play at convective boundaries can be difficult in numerical simulations. Downward flows (or plumes) crossing a convective boundary at the bottom of an envelope are clearly observed in numerical simulations (see e.g. Baraffe et al. 2021). Ballistic plume crossings may eventually lead to a modification of the thermal background – the so-called *penetration* process. But for such modification to be observed, simulations must be run over many thousands of convective turnover time-scales, as theoretically expected and recently demonstrated in simulations by Anders et al. (2022) based on three-dimensional (3D) simulations of convection in a Cartesian box with idealized set-ups. In a numerical study of solar-like convective envelopes, Baraffe et al. (2021) show that artificially boosting the luminosity of the stellar model by a factor 10^4 yields a significant modification of the thermal background below the convective boundary with an extension of the size of the layer characterized by the penetration of convective flows, which could lead to a growth of the convectively unstable zone down to deeper levels. Whether this growth stabilizes or whether the convective boundary continues moving downward indefinitely is unclear. For the solar-like model with realistic stellar luminosity, a slight modification

of the thermal background is also observed in the simulations of Baraffe et al. (2021), but they show no trend of an extension of the Schwarzschild convective boundary over the simulation time.

Following the approach developed in Pratt et al. (2017) for convective envelopes, the most vigorous plumes can be used to define a maximal overshooting length, which can be significantly deeper than the typical length reached by the bulk of the plumes (Pratt et al. 2017; Baraffe et al. 2021; Vlaykov et al. 2022). Whether this ballistic process is also observed for convective cores and can drive significant mixing is an open question. Arguments based on the dynamics of convective motions and plumes suggest that mixing below a convective zone (e.g. envelope overshooting) and above (e.g. core overshooting) may indeed be different (Andrássy & Spruit 2013). Simple arguments based on the kinetic energy of a plume with typical velocity and the restoring buoyancy force suggest very small overshooting lengths for the cores of low- and intermediate-mass zero-age main-sequence (ZAMS) stars (Higl, Müller & Weiss 2021). But these estimates are based on typical velocities without considering possible extreme plume events. The situation could also be different for convective cores on the ZAMS and on the main sequence. Indeed, the building of a molecular weight gradient at the core boundary due to hydrogen burning in the core can hamper the lifting of heavier material by ballistic processes. An entrainment process slowly eroding the convective boundary may thus dominate at some point over the ballistic process during the main-sequence evolution, or both processes may coexist and contribute to mixing. These questions are still unsettled. Existing numerical simulations of convective cores have mostly focused on one single stellar mass model, rather than a range of stellar masses (Meakin & Arnett 2007; Gilet et al. 2013; Rogers et al. 2013; Edelmann et al. 2019; Horst et al. 2020; Higl et al. 2021). Additionally, many of these works enhance the stellar luminosity of the model, to provide numerical stability, or to accelerate the thermal relaxation or the Mach number of the convective flow. This artefact may artificially favour one process over the other. At this time, it is difficult to draw any firm conclusion regarding the main mechanisms that drive CBM in stars and how their efficiency is affected with stellar mass and with the stage of evolution on the main sequence.

In this work devoted to convective cores, we study the efficiency for convective plumes to penetrate into the stable region as a function of stellar mass for ZAMS models. In the following, we will refer to overshooting to describe this process, since we essentially describe the ballistic process and even if a modification of the temperature gradient is observed for the most luminous models (see Section 5), likely leading to *penetration* as defined by Zahn (1991). We perform two-dimensional (2D) numerical simulations of convective cores of ZAMS stellar models covering a range of stellar masses between 3 and 20 M_{\odot} (Section 2). Our goal is to apply the framework of extreme plume events developed for convective stellar envelopes (Pratt et al. 2017, 2020; Baraffe et al. 2021) to the convective cores of intermediate-mass and massive stars. We analyse whether extreme events can provide overshooting lengths required for stellar models to reproduce observations. For this purpose, we derive a relationship between overshooting length and stellar luminosity based on present numerical simulations (Section 4). We apply the relationship to one-dimensional (1D) stellar evolution models and test them against observations (Section 6). This is the first step for a systematic study devoted to convective core overshooting in intermediate-mass and massive stars.

Table 1. Properties of the initial stellar models (all models have a central helium abundance $Y_c = 0.2838$) used for the 2D hydrodynamical simulations: total mass, stellar luminosity, stellar radius, mass and radius of the convective core (corresponding to the location of the Schwarzschild boundary), and the pressure scale height at the Schwarzschild boundary.

M/M_\odot	$L_{\text{star}}/L_\odot^a$	R_{star} (cm)	M_{conv}/M_\odot	$r_{\text{conv}}/R_{\text{star}}$	$H_{P,\text{CB}}$ (cm)
3	7.7673×10	1.3855×10^{11}	0.5724	0.1486	1.3×10^{10}
5	5.2186×10^2	1.8424×10^{11}	1.212	0.1814	1.8×10^{10}
10	5.5726×10^3	2.7295×10^{11}	3.046	0.2239	2.7×10^{10}
15	1.9242×10^4	3.4255×10^{11}	5.600	0.2580	3.3×10^{10}
20	4.2962×10^4	4.0172×10^{11}	8.7947	0.2869	3.7×10^{10}

^aWe use $L_\odot = 3.839 \times 10^{33}$ erg s⁻¹.

2 NUMERICAL SIMULATIONS

We use the fully compressible time-implicit code MUSIC. A full description of MUSIC and of the time-implicit integration can be found in Viallet, Baraffe & Walder (2011), Viallet et al. (2016), and Goffrey et al. (2017). MUSIC solves the inviscid Euler equations in the presence of external gravity and thermal diffusion:

$$\frac{\partial \rho}{\partial t} = -\nabla \cdot (\rho \mathbf{v}), \quad (1)$$

$$\frac{\partial \rho \mathbf{v}}{\partial t} = -\nabla \cdot (\rho \mathbf{v} \otimes \mathbf{v}) - \nabla p + \rho \mathbf{g}, \quad (2)$$

$$\frac{\partial \rho e}{\partial t} = -\nabla \cdot (\rho e \mathbf{v}) - p \nabla \cdot \mathbf{v} + \nabla \cdot (\chi \nabla T) + Q_{\text{nuc}}, \quad (3)$$

where ρ is the density, e the specific internal energy, \mathbf{v} the velocity, p the gas pressure, T the temperature, \mathbf{g} the gravitational acceleration, and χ the thermal conductivity. The term Q_{nuc} represents the nuclear energy rate. The symbol \otimes is the outer product. All hydrodynamical simulations presented in this work are performed assuming spherically symmetric gravitational acceleration \mathbf{g} , which is updated every time interval Δt .¹ All simulations presented in this work are performed with $\Delta t = 10^3$ s. The typical dynamical time-scale of the entire stellar cores analysed in this study $\tau_{\text{dyn}} \sim 1/\sqrt{(\rho_{\text{mean}} G)}$, with ρ_{mean} the mean density of the core and G the gravitational constant, is of the order of 10^3 s. We have checked with a number of test simulations that a variation of Δt between 10^2 and 10^5 s does not impact our results.

In the stellar models considered, radiative transfer is the major heat transport that contributes to the thermal conductivity, which is given for photons by

$$\chi = \frac{16\sigma T^3}{3\kappa\rho}, \quad (4)$$

where κ is the Rosseland mean opacity and σ the Stefan–Boltzmann constant. Realistic stellar opacities and equation of states appropriate for the description of stellar interiors are implemented in MUSIC. Opacities are interpolated from the OPAL tables (Iglesias & Rogers 1996) for solar metallicity and the equation of state is based on the OPAL equation-of-state tables of Rogers & Nayfonov (2002).

¹Note that Δt is the time after which the gravitational potential is updated, not the numerical time-step. The numerical time-step used for these simulations is set by the hydrodynamical CFL (Courant-Friedrich-Levy) number varying between 10 and 50 (see Viallet et al. 2011, for definitions) and corresponding to values for the time-step ranging between 5 and 40 s.

2.1 Initial stellar models

To provide the initial structures for the 2D simulations, we compute stellar models in the mass range 3–20 M_\odot with the 1D Lyon stellar evolution code (Baraffe & El Eid 1991; Baraffe et al. 1998), using the same opacities and equation of state as MUSIC.² The 2D simulations require as initial input a radial profile of density and internal energy. The 1D stellar evolution models have an initial helium abundance in mass fraction $Y = 0.28$ and solar metallicity $Z = 0.02$ and were computed through the pre-main-sequence and main-sequence phases. All initial models for the 2D simulations in this study are taken at the beginning of core hydrogen burning and have a central abundance of helium $Y_c = 0.2838$, i.e. only ~ 1 percent of their central hydrogen has been depleted. There is thus a very shallow mean molecular weight gradient at the convective boundary. Follow-up analyses of later stages of evolution with a steeper gradient of molecular weight at the core boundary are in progress (Morison et al., in preparation). Convective stability is defined by the Schwarzschild criterion $\nabla < \nabla_{\text{ad}}$, with $\nabla = \frac{d \log T}{d \log P}$ the temperature gradient and $\nabla_{\text{ad}} = \frac{d \log T}{d \log P} \Big|_S$ the adiabatic gradient. The 1D stellar models used to generate the initial structures for the 2D simulations do not account for overshooting at the convective core boundary. In the following, we define the Schwarzschild boundary as the transition layer between convective instability ($\nabla > \nabla_{\text{ad}}$) and stability ($\nabla < \nabla_{\text{ad}}$). The properties of the initial 1D stellar structures are provided in Table 1. Nuclear energy generated in the convective cores is accounted for in the internal energy equation (equation 3) through the term Q_{nuc} using the radial profile of the nuclear energy rate from the 1D stellar model. Given that the simulation times are orders of magnitude smaller than the nuclear time-scale for H burning in the cores, the nuclear energy is assumed to remain constant with time.

2.2 Spherical-shell geometry and boundary conditions

2D simulations are performed in a spherical shell using spherical coordinates, namely r the radius and θ the polar angle, and assuming azimuthal symmetry in the ϕ -direction. For all models, the inner radius r_{in} is defined at $0.02 R_{\text{star}}$. The choice of the outer radius r_{out} depends on the stellar model. Since the main motivation of this work is to analyse the extent of the overshooting layer for different stellar masses, the outer radius r_{out} is fixed at a distance of $\sim 1 \times H_{P,\text{CB}}$ for the lowest mass (3 M_\odot) to $\sim 3.5 \times H_{P,\text{CB}}$ for the highest mass (20 M_\odot) away from the convective boundary r_{conv} . Extension of the radial domain to analyse the generation of internal waves at the core boundary and their propagation in the radiative envelope

²The 1D initial structures are available on the repository: http://perso.ens-lyon.fr/isabelle.baraffe/2Dcore_overshooting_2023.

Table 2. Main properties of the 2D simulations.

Model	M/M_{\odot}	L (erg s $^{-1}$)	$N_r \times N_{\theta}$	$r_{\text{out}}/R_{\text{star}}$	$\tau_{\text{conv}}^{\text{a}}$ (s)	$N_{\text{conv}}^{\text{b}}$	$t_{\text{steady}}^{\text{c}}$ (s)	$t_{\text{sim}}^{\text{d}}$ (s)
3L0	3	2.981×10^{35}	336 x 168	0.25	1.9×10^6	1442	9.5×10^8	3.71×10^9
3L1	3	2.981×10^{36}	336 x 168	0.25	8×10^5	1211	4.6×10^8	1.43×10^9
3L2	3	2.981×10^{37}	336 x 168	0.25	3.9×10^5	501	9×10^7	2.84×10^8
3L2xhres	3	2.981×10^{37}	684 x 342	0.25	3.8×10^5	514	9×10^7	2.84×10^8
3L3	3	2.981×10^{38}	336 x 168	0.25	1.7×10^5	1904	6×10^7	3.81×10^8
3L3xhres	3	2.981×10^{38}	684 x 342	0.25	1.7×10^5	1243	6×10^7	2.71×10^8
3L4	3	2.981×10^{39}	336 x 168	0.25	8.9×10^4	1457	3×10^7	1.60×10^8
3L4xhres	3	2.981×10^{39}	684 x 342	0.25	8.7×10^4	1400	3×10^7	1.52×10^8
5L0	5	2.003×10^{36}	400 x 200	0.3	1.4×10^6	1260	2.45×10^8	2.01×10^9
10L0	10	2.139×10^{37}	416 x 208	0.4	1.2×10^6	1260	2.1×10^8	1.77×10^9
15L0	15	7.387×10^{37}	688 x 344	0.5	1.1×10^6	875	10^8	1.14×10^9
20L0	20	1.649×10^{38}	864 x 430	0.6	1.1×10^6	800	9×10^7	9.99×10^8

^aConvective turnover time (see Section 3 for its definition).

^bNumber of convective turnover times covered by the simulation once steady state convection is reached.

^cPhysical time to reach a steady state for convection.

^dTotal physical runtime of the simulation.

is the work in progress. The angular extent ranges from $\theta = 0^\circ$ to $\theta = 180^\circ$. The grid has uniform spacing in the r and θ coordinates. The choice for the resolution (N_r, N_{θ}) is set by the condition to have a good resolution of the pressure scale height at the Schwarzschild boundary. Effective Reynolds and Prandtl numbers are commonly used to set the resolution of numerical simulations. But given that our simulations are based on an implicit large eddy simulation approach, only a rough estimate can be provided for these numbers. They will in any case remain far away from the conditions prevailing in stellar interiors. We suggest that a more relevant resolution criterion for hydrodynamical simulations devoted to the study of overshooting using realistic stellar structures should be the number of grid cells per pressure scale height at the convective boundary. This should allow a more relevant comparison between the works of different groups devoted to the study of different stars. We use ~ 110 – 140 grid cells per pressure scale height in the radial direction. The details of the resolution adopted in this work are provided in Table 2. We have also performed a few tests with higher resolution and analyse the impact in Section 4.

The radial boundary conditions for the density correspond to a constant radial derivative on the density (see Pratt et al. 2016). The energy flux at the inner and outer radial boundaries are set to the value of the energy flux at that radius in the 1D stellar evolution model. At the boundaries in θ , because of the extension of the angular domain to the poles, reflective boundary conditions for the density and the energy are used (i.e. the values are mirrored at the boundary). For the velocity, we impose reflective conditions at the radial and polar boundaries, corresponding to

- (i) $v_r = 0$ and $\frac{\partial v_{\theta}}{\partial r} = 0$ at r_{in} and r_{out} ,
- (ii) $\frac{\partial v_r}{\partial \theta} = 0$ and $v_{\theta} = 0$ at $\theta = 0^\circ$ and $\theta = 180^\circ$.

We have also performed simulations for the $3 M_{\odot}$ model with artificial enhancement of the stellar luminosity and the thermal diffusivity by factors $10, 10^2, 10^3$, and 10^4 . This covers the range of luminosities of the stellar masses considered in this work (3 – $20 M_{\odot}$). This choice of enhancement factor allows a comparative analysis of the impact of the luminosity for fixed core mass and increasing core mass. Note that even larger enhancement factors (up to 10^7) for a $3 M_{\odot}$ stellar structure can be found in previous works (e.g. Rogers et al. 2013; Edelmann et al. 2019). For the artificially boosted simulations, the energy flux (equivalently, the luminosity) at the radial boundaries

is multiplied by the enhancement factor, the nuclear energy rate is multiplied by the same factor, and the Rosseland mean opacities κ in MUSIC are decreased by the same factor.

3 RESULTS: AVERAGE DYNAMICS

The properties of all simulations are summarised in Table 2. We define t_{steady} as the time required to reach a steady state for convection, characterized by the total kinetic energy E_{kin} of the system reaching a plateau. Before t_{steady} , the initial relaxation phase is characterized by the propagation of strong acoustic waves and the onset of convection. At t_{steady} , the value of the kinetic energy starts to stabilize and from this time it remains roughly constant with time (following the dotted curve that corresponds to the value of E_{kin} at t_{steady} for each model). The simulations are stopped at time t_{sim} provided in Table 2. None of these simulations are thermally relaxed, given that the total simulation times for all models are orders of magnitude smaller than the relevant thermal time-scale $\sim GM^2/(R_{\text{star}}L)$. As a consequence, all these simulations are expected to maintain a secular drift. We have compared the radial profile of the internal energy, averaged in the angular direction, for each 2D model at time t_{steady} and at time t_{sim} . We find a maximum of 0.5 per cent relative difference for the internal energy at a given radius, with the largest difference found for the most luminous models (see Section 5). The above-mentioned drift is thus so slow that calculating statistical or averaged data during this very slowly changing transitional state is sensible.

Fig. 1 shows the evolution of the total kinetic energy as a function of time for all models and the plateau characterizing their steady state. The initial transient phase can last a relatively long time, depending on the model studied. For the model 3L0, we note a different behaviour. After the peak due to strong acoustic waves, the kinetic energy continuously decreases until $t \sim 2.4 \times 10^8$ s ($\log t \sim 8.38$). In this regime, convection develops in the core (within the 1D Schwarzschild boundary) in two spatially separate regions. The abrupt increase of E_{kin} observed at $t \sim 2.4 \times 10^8$ s marks the merging of these two convective regions and the beginning of fully developed convection in the core. The Mach number characterizing the convective velocities in model 3L0 is small, of the order of $\sim 10^{-4}$, which is numerically challenging. This low Mach number explains why several previous works artificially enhance the luminosity of the model (Rogers et al. 2013; Horst et al. 2020). There is no need for this artefact for the model 3L0 as MUSIC’s numerical scheme

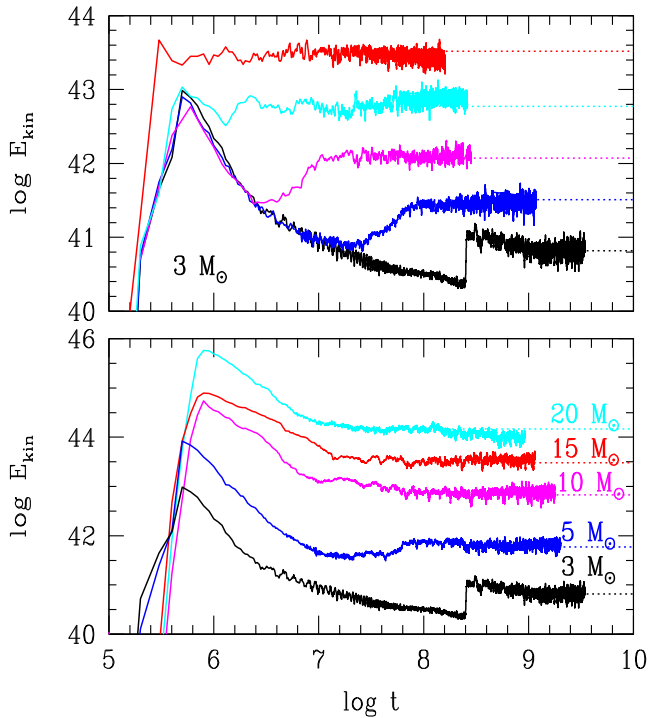


Figure 1. Evolution of the total kinetic energy (in erg; y-axis with a base-10 log scale) as a function of time (in s) for the simulations described in Table 2. Top panel: results for $3 M_{\odot}$ models with various luminosity enhancement factors: 3L0 (black), 3L1 (blue), 3L2 (magenta), 3L3 (cyan), and 3L4 (red). Bottom panel: results for a range of stellar masses. The dotted line for each model corresponds to the value of the total kinetic energy at the beginning of the steady state for convection.

allows convection to develop and eventually reach a steady state even after a long transient phase. Note that this unusual transient phase observed for the model 3L0 will likely change with a different procedure for initializing the simulation. All simulations start without an imposed background noise (i.e. initial velocities are set to zero). Imposing initially a background noise for the model 3L0 may change the location where convection starts and thus the behaviour of the transient phase, which is irrelevant for the analysis performed in the following. A global convective turnover time τ_{conv} is estimated based on the rms velocity $v_{\text{rms}}(r, t)$ at radius r and time t , which characterizes a bulk convective velocity. We define τ_{conv} by

$$\tau_{\text{conv}} = \left\langle \int_{r_{\text{in}}}^{r_{\text{conv}}} \frac{dr}{v_{\text{rms}}(r, t)} \right\rangle_t, \quad (5)$$

where the rms velocity is given by

$$v_{\text{rms}}(r, t) = \sqrt{\langle v^2(r, \theta, t) \rangle_{\theta}}, \quad (6)$$

with $v^2 = v_r^2 + v_{\theta}^2$, v_r and v_{θ} being the radial and angular velocities, respectively. Time averages are denoted by $\langle \rangle_t$ and calculated between t_{steady} and t_{sim} , the final time reached by the simulation (see values in Table 2). For any quantity X , we define

$$\langle X \rangle_t = \frac{1}{(t_{\text{sim}} - t_{\text{steady}})} \int_{t_{\text{steady}}}^{t_{\text{sim}}} X dt. \quad (7)$$

The volume-weighted average in the angular direction $\langle \rangle_{\theta}$ is defined for any quantity X as

$$\langle X(r, \theta, t) \rangle_{\theta} = \frac{\int_{\theta} X(r, \theta, t) dV(r, \theta)}{\int_{\theta} dV(r, \theta)}. \quad (8)$$

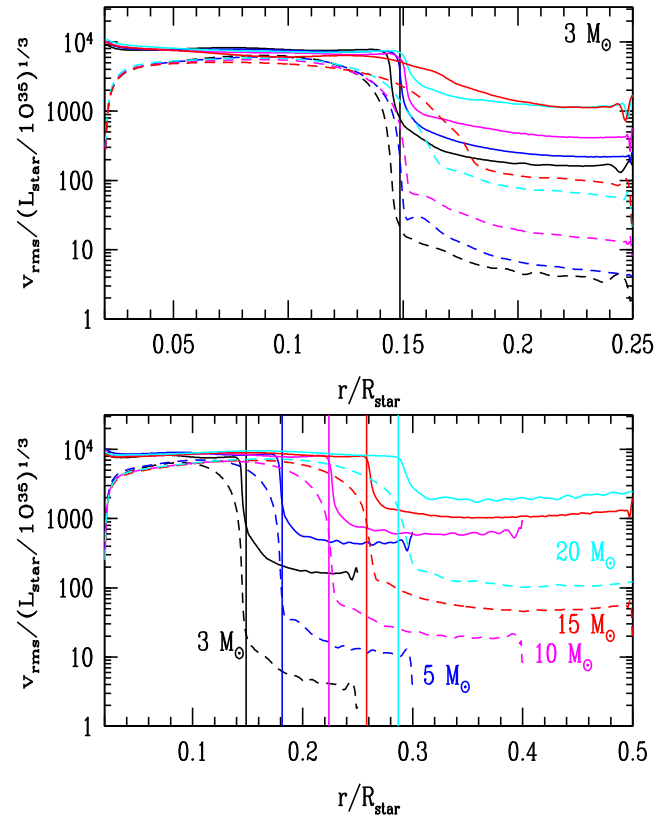


Figure 2. Radial profile of the time-averaged rms velocity (solid lines) and rms radial velocity (dashed lines) scaled by $(L_{\text{star}}/10^{35})^{1/3}$. Top panel: results for $3 M_{\odot}$ models with various luminosity enhancement factors: 3L0 (black), 3L1 (blue), 3L2 (magenta), 3L3 (cyan), and 3L4 (red). Bottom panel: results for a range of stellar masses: 3L0 (black), 5L0 (blue), 10L0 (magenta), 15L0 (red), and 20L0 (cyan). The convective boundary corresponding to the Schwarzschild boundary from the 1D initial model is indicated by a vertical solid line with the colour corresponding to each stellar mass.

The simulations are stopped after a time t_{sim} when convergence of the statistics used to determine the size of the layer penetrated by plumes is obtained, as explained in the next section (Section 4). Table 2 provides the values and numbers of the convective turnover times. Fig. 2 displays the rms velocity and rms radial velocity for the $3 M_{\odot}$ models with artificially enhanced luminosities (top panel) and for the range of stellar masses investigated (bottom panel), scaled by $L_{\text{star}}^{1/3}$. In the convective core, our simulations reproduce the expected scaling of convective velocity with luminosity $v_{\text{conv}} \propto L^{1/3}$ recovered by many hydrodynamical simulations (e.g. Jones et al. 2017; Edelmann et al. 2019; Andrassey et al. 2020; Horst et al. 2020; Baraffe et al. 2021; Higl et al. 2021). This scaling is expected from mixing-length theory (MLT) based on the argument that the turbulent dissipation rate of kinetic energy in a turbulent convective zone scales with v^3 (Biermann 1932). But a general scaling of the total flux with v^3 can also be derived for the kinetic energy and the enthalpy fluxes based on simple dimensional arguments (see Jones et al. 2017).

The rms velocities in the stably stratified region are due to the penetrative flows just above the convective boundary and to the propagation of internal waves excited by the convective motions and the penetrating plumes. The top panel of Fig. 2 shows that these velocities also increase with the luminosity, suggesting more efficient overshooting of the convective motions above the convective boundary and thus larger overshooting length with increasing

luminosity. Baraffe et al. (2021) reports similar behaviours for convective envelopes of solar-like models with artificially enhanced luminosities. Quantitative estimate of the overshooting lengths for all models is performed in Section 4.

4 RESULTS: EXTENT OF THE OVERSHOOTING REGION

4.1 Determination of overshooting lengths

To determine an overshooting length, we adopt the same approach as in Baraffe et al. (2021) and initially inspired by the findings of Pratt et al. (2017). This approach is based on the analysis of the depth of all convective plumes that penetrate beyond the convective boundary. The two criteria used to determine the depth of a penetrative plume at a given angle θ and time t are based on the first zero above the convective boundary r_{conv} of the vertical kinetic energy flux f_k and vertical heat flux $f_{\delta T}$, defined by (see Pratt et al. 2017)

$$f_k(r, \theta, t) = \frac{1}{2} \rho(r, \theta, t) v^2(r, \theta, t) v_r(r, \theta, t), \quad (9)$$

$$f_{\delta T}(r, \theta, t) = \rho(r, \theta, t) c_p(r, \theta, t) \delta T(r, \theta, t) v_r(r, \theta, t), \quad (10)$$

where c_p is the specific heat at constant pressure and the temperature fluctuation δT is defined by

$$\delta T(r, \theta, t) = T(r, \theta, t) - \langle \langle T(r, \theta, t) \rangle \rangle_{\theta, t}. \quad (11)$$

The method is the same as the one developed in Baraffe et al. (2021) for convective envelopes. At each time t , we calculate at each angle θ the radial positions $r_0(\theta, t)$ of a plume corresponding to the first zero of f_k and $f_{\delta T}$, respectively, above the convective boundary r_{conv} . The corresponding overshooting length l_0 with respect to r_{conv} is defined by

$$l_0(\theta, t) = r_0(\theta, t) - r_{\text{conv}}. \quad (12)$$

Fig. 3 illustrates the angular structure of the overshooting layer at an arbitrary time for the 10 M_{\odot} stellar model.

We then define the maximal overshooting length l_0^{max} at a given time by the maximum over all angles θ :

$$l_0^{\text{max}}(t) = \max(l_0(\theta, t)). \quad (13)$$

The time average $l_{\text{max}} = \langle l_0^{\text{max}}(t) \rangle_t$ provides an effective width for the overshooting layer where the most vigorous plumes penetrate and which we use to characterize the extension of the mixing layer over the long-term evolution of the star (Pratt et al. 2017; Baraffe et al. 2021). Table 3 displays l_{max} based on the criterion for f_k and $f_{\delta T}$, respectively, for all models. The distributions of overshooting lengths derived from f_k and $f_{\delta T}$, respectively, slowly converge with time, as found in Pratt et al. (2017) and Baraffe et al. (2021). Several hundreds to thousand convective turnover times, depending on the stellar model, are required for the statistics to converge. Eventually, both criteria provide similar values for the effective overshooting width. The values of the overshooting width based on $f_{\delta T}$ converge faster with time, compared to the value based on f_k , as found as well for convective envelopes in Baraffe et al. (2021). The values of $l_{\text{max}}(f_{\delta T})$ provided in Table 3 have reached a steady state for all models after t_{sim} . Depending on the stellar model, $l_{\text{max}}(f_k)$ gets close to $l_{\text{max}}(f_{\delta T})$ (difference of $\lesssim 20$ per cent) for all models but models 3L0 and 20L0, for which $l_{\text{max}}(f_k)$ continues to slowly decrease even after more than $800 \times \tau_{\text{conv}}$. We run three simulations for the 3 M_{\odot} models with enhanced luminosity with twice the resolution in both radial and angular directions and covering about the same simulation

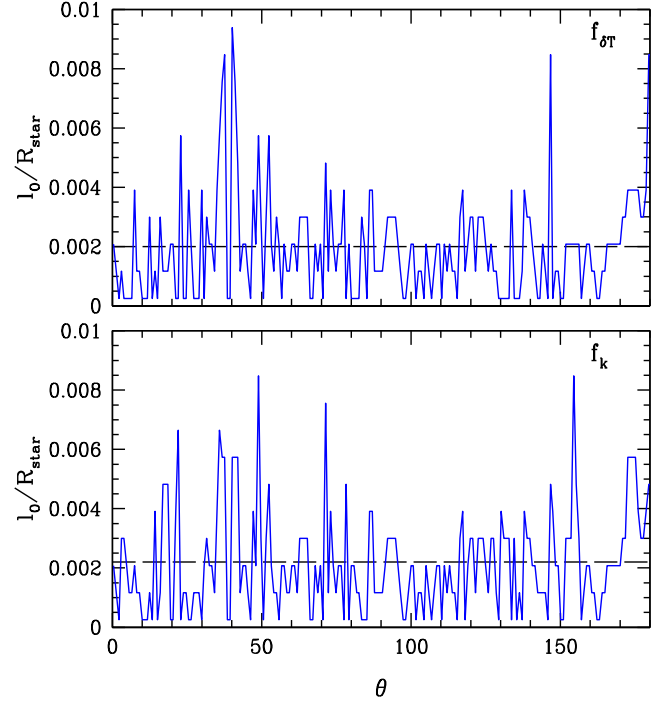


Figure 3. Overshooting lengths l_0 defined by equation (12) as a function of the angle θ at time $t = 8.3 \times 10^8$ s for the 10 M_{\odot} model. The upper panel corresponds to l_0 defined by f_k and the lower panel to l_0 defined by $f_{\delta T}$. The horizontal dashed line in each panel indicates the average overshooting length at this time.

time as their lower resolution counterpart, in order to check the sensitivity of the values of l_{max} to the resolution. The properties of these higher resolution models (labelled 2xhres) are displayed in Table 2. The results for the overshooting lengths are given in Table 3 and show similar values for $l_{\text{max}}(f_{\delta T})$ as found with a lower resolution. The values for $l_{\text{max}}(f_k)$ of the higher resolution models are larger than the corresponding values for the lower resolution model, as it takes more time for $l_{\text{max}}(f_k)$ in the high-resolution models to decrease to the level of $l_{\text{max}}(f_{\delta T})$. But the value of $l_{\text{max}}(f_k)$ in the high-resolution models continues to decrease with time and we expect it to eventually converge and thus get much closer to $l_{\text{max}}(f_{\delta T})$ and to the value of $l_{\text{max}}(f_k)$ found in the lower resolution model.

4.2 Relationship between overshooting length and stellar luminosity

The variation of l_{max} with the stellar luminosity is illustrated in Fig. 4 for the 3 M_{\odot} models with enhanced luminosity and for the set of stellar masses with realistic luminosity. As expected from the behaviour of the rms velocities (see Fig. 2), overshooting lengths increase with the stellar luminosity. To derive an approximate scaling relationship for the overshooting length d_{ov} that can be implemented in stellar evolution codes, we use the values of l_{max} derived from $f_{\delta T}$, since these values have converged with time. We derive the following expression, which fits the results for the stellar mass range studied:

$$d_{\text{ov}}/H_{P,\text{CB}} = 3.05 \times 10^{-3} \times (L/L_{\odot})^{1/3} \times (r_{\text{conv}}/H_{P,\text{CB}})^{1/2} + 0.02. \quad (14)$$

We find a typical scaling with the luminosity $d_{\text{ov}} \propto L^{1/3} \propto v_{\text{conv}}$. Numerical studies of convective envelopes report overshooting lengths d_{ov} that vary with the luminosity following $d_{\text{ov}} \propto L^a$ with

Table 3. Effective width l_{\max} of the overshooting layer in units of the total stellar radius and of the pressure scale height at the convective boundary, for all models considered in this study. The quantity $l_{\max}(f_k)$ is based on the criterion using f_k (equation 9) and $l_{\max}(f_{\delta T})$ is based on $f_{\delta T}$ (equation 10).

Model	$l_{\max}(f_k)/R_{\text{star}}$	$l_{\max}(f_{\delta T})/R_{\text{star}}$	$l_{\max}(f_k)/H_{P,\text{CB}}$	$l_{\max}(f_{\delta T})/H_{P,\text{CB}}$
3L0	6.4×10^{-3}	3.7×10^{-3}	6.8×10^{-2}	3.9×10^{-2}
3L1	4.2×10^{-3}	4.2×10^{-3}	4.5×10^{-2}	4.5×10^{-2}
3L2	6.2×10^{-3}	6.1×10^{-3}	6.6×10^{-2}	6.5×10^{-2}
3L2xhres	8.4×10^{-3}	6.4×10^{-3}	8.9×10^{-2}	6.8×10^{-2}
3L3	1.8×10^{-2}	1.6×10^{-2}	1.9×10^{-1}	1.7×10^{-1}
3L3xhres	2.2×10^{-2}	1.6×10^{-2}	2.3×10^{-1}	1.7×10^{-1}
3L4	3.5×10^{-2}	2.8×10^{-2}	3.7×10^{-1}	3.0×10^{-1}
3L4xhres	4.0×10^{-2}	3.0×10^{-2}	4.2×10^{-1}	3.2×10^{-1}
5L0	9.3×10^{-3}	6.0×10^{-3}	9.5×10^{-2}	6.1×10^{-2}
10L0	1.2×10^{-2}	1.1×10^{-2}	1.2×10^{-1}	1.1×10^{-1}
15L0	1.6×10^{-2}	1.3×10^{-2}	1.66×10^{-1}	1.35×10^{-1}
20L0	3.5×10^{-2}	2.0×10^{-2}	3.8×10^{-1}	2.17×10^{-1}

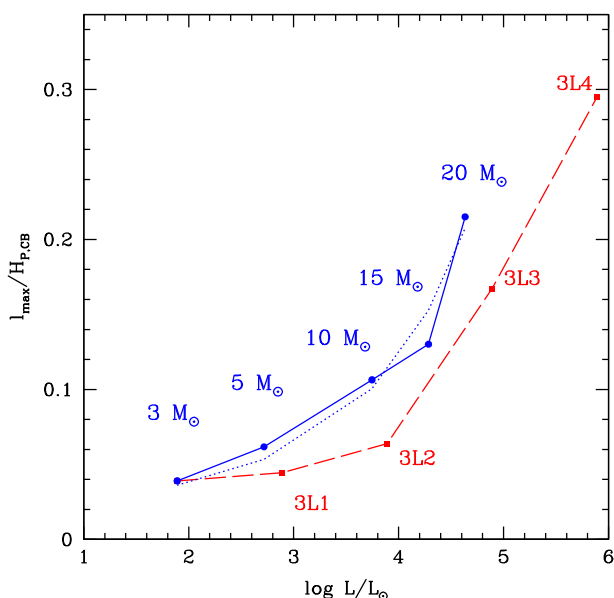


Figure 4. Overshooting length l_{\max} , in units of the pressure scale height at the convective boundary, as a function of the model luminosity. The $3 M_{\odot}$ models with various luminosity enhancement factors are indicated in red (dashed line). The results for a range of stellar masses with realistic stellar luminosity are indicated in blue (solid line). The dotted curve shows the fit for the overshooting length $d_{\text{ov}}/H_{P,\text{CB}}$ given by equation (14).

a varying between 0.08 and 0.31 (Hotta 2017; Käpylä 2019; Baraffe et al. 2021). The analytical model of Zahn (1991) for penetration, based on first-order estimate of the deceleration of a plume in an adiabatically stratified penetration zone, predicts $d_{\text{ov}} \propto v_{\text{conv}}^3$. Our results also show that the overshooting lengths derived for a fixed stellar mass (and thus a fixed convective core size) are systematically smaller than the ones derived for larger cores but similar luminosity. Interestingly, a dependence of d_{ov} with the size of the core r_{conv} is also predicted by Zahn (1991) (see their equation 4.5) with the same relation of proportionality $d_{\text{ov}} \propto (r_{\text{conv}}/H_{P,\text{CB}})^{1/2}$ as found in present simulations. This dependence in the Zahn model is derived from the strong variations with radius of various relevant quantities such as the gravitational acceleration g , the mass $m(r)$ enclosed in a sphere of radius r , the radiative conductivity χ , and thus the radiative flux, close to the convective core boundary. In our simulations, we expect

the radial dependence of the gravitational acceleration to have the main impact. We find that the larger the core (in terms of radius and mass), the smaller the gravitational acceleration at the core boundary $g_{\text{conv}} \sim GM_{\text{conv}}/r_{\text{conv}}^2$ (see values in Table 1). Therefore, the larger the stellar mass, the larger the velocities at the convective boundary and the smaller the restoring force due to gravity, implying upflows to penetrate over larger distances. This is a plausible explanation for the dependence of d_{ov} on the convective core radius. We analyse below (Section 6) whether the expression provided by equation (14) provides a reasonable agreement between stellar evolution models and observations.

5 THERMAL BACKGROUND EVOLUTION

The prescription used in the previous section to determine overshooting lengths relies on two assumptions. First, we consider that the simulations have reached a steady state for convection (i.e. a global dynamical steady state). This assumption is reasonable based on the observation that the total kinetic energy of the system reaches a plateau as a function of time (see Fig. 1). Secondly, we assume that the relevant convective boundary from which the overshooting lengths are defined is the 1D Schwarzschild boundary. This is directly useful for the purpose of implementing these overshooting lengths in 1D stellar evolution codes. However, we find that in all models a small nearly adiabatic layer just above the convective boundary forms rapidly once convection steady state is reached. For the most luminous models, we observe that this small layer slowly grows in size with time.

Anders et al. (2022) also find a modification of the temperature gradient, which becomes close to the adiabatic gradient in the penetration layer. They report that their simulations exhibit the process of convective penetration as defined by e.g. Zahn (1991), with convective penetrating motions mixing entropy and establishing a nearly adiabatic stratification above the Schwarzschild boundary (see also Brummell, Clune & Toomre 2002). Anders et al. (2022) suggest that the extent of convective penetration is limited and derive arguments involving the convective flux, the viscous dissipation rate, and the buoyancy work, providing an estimate of the penetration width. Depending on their set-up, they find that penetration zones can take thousands of convective turnover times to saturate. They show properties of the flow and of the temperature fluctuations close to a convective boundary (see their fig. 1), which are similar

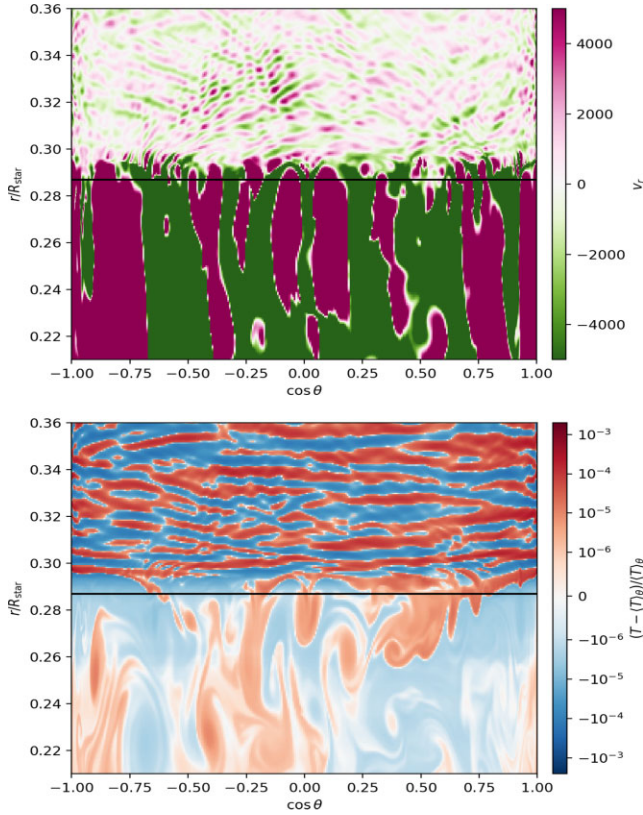


Figure 5. Visualization of the radial velocity v_r [cm s^{-1}] (top panel) and the relative temperature fluctuations $(T - \langle T \rangle_\theta) / \langle T \rangle_\theta$ (bottom panel) in a region zoomed around the convective boundary (horizontal black line) for the model 20L0 at time $t = 7 \times 10^8$ s. The x -axis represents the co-latitude (in terms of $\cos \theta$). Note that to better illustrate upwellings and downwellings in the top panel, the velocity scale is saturated, i.e. any velocity $> v_{r,\text{max}} = 5 \times 10^3$ cm s^{-1} ($< v_{r,\text{min}} = -5 \times 10^3$ cm s^{-1}) is represented with the same colour as $v_{r,\text{max}}$ ($v_{r,\text{min}}$).

to our results, as illustrated in Fig. 5 for the model 20L0 at a given time. As expected in convective regions, convective upflows transport hot material from the central regions up to the top of the convective core. Inspection of temperature fluctuations (i.e. the difference between the local temperature and the horizontally averaged background) indeed indicates that upflows in the convective region are characterized by positive temperature fluctuations and downflows by negative temperature fluctuations. When upflows cross the convective boundary, at the top of the convective core, and penetrate the stably stratified medium, they adiabatically expand and therefore get cooler (negative temperature fluctuation) and denser than the subadiabatically stratified environment.

To understand the establishment of a nearly adiabatic layer in the penetration region, one needs to compare the advection time-scale, which characterizes the process of entropy mixing by penetrating flows (i.e. an advection process), and the thermal diffusion time-scale. If penetrating flows, as illustrated in the top panel of Fig. 5, can drive efficient entropy/thermal mixing, the layer characterized by penetrating upflows will remain nearly adiabatic if thermal diffusion is slow enough. Table 4 provides estimates of the diffusive time-scale $\tau_{\text{diff}} = L^2 / \kappa_{\text{rad}}$ at the core boundary, with L a relevant length-scale and $\kappa_{\text{rad}} = \chi / (\rho c_p)$ the thermal diffusivity (which is the radiative diffusivity for present stellar models with χ defined in equation 4). Estimate of an advection time-scale $\tau_{\text{adv}} = L / v_{r,\text{rms}}$ is based on

the time-averaged rms radial velocity at the core boundary. For the characteristic length-scales at the core boundary, we use the overshooting distance $l_{\text{max}}(f_{\delta T})$ (see Table 3) and the pressure scale height H_P (see Table 1). As illustrated in Table 4, typical advection time-scales are much smaller than typical thermal diffusion time-scales for all models.

The growth in size with time of the nearly adiabatic layer observed in the most luminous models is illustrated in Fig. 6 for the models 3L3 and 3L4. This growth with time may also happen in the less luminous models, but their very slow evolution and less vigorous penetrating flows may prevent clearly exhibiting this feature over present simulation times.

We also note that the angular averaged temperature gradient in the models, while getting very close to the adiabatic gradient, remains stable against the Schwarzschild criterion over the simulation times.

For the purpose of analysing the time evolution of the nearly adiabatic layer, we have extended the simulation time of the models 3L3 and 3L4 beyond the value of t_{sim} used to determine overshooting depths (see Table 2), until $t_{\text{final}} = 5 \times 10^8$ s ($\sim 2600 \times \tau_{\text{conv}}$ for 3L3 and $\sim 5300 \times \tau_{\text{conv}}$ for 3L4). The aim is to reach a simulation time for these models close to or greater than the thermal diffusion time-scale in the overshooting layer $\tau_{\text{diff}}(l_{\text{max}})$. Given the smaller grid size and larger thermal diffusivity of these models, this is still computationally affordable. Fig. 6 shows clearly in models 3L3 and 3L4 that the radial extension of the nearly adiabatic layer slows down with time as the upper edge gets closer to the location of l_{max} . Since the change of the temperature gradient is driven by penetrating flows, one may expect that the nearly adiabatic layer would not extend beyond l_{max} and that its growth may slow down when thermal diffusion starts to play a role. This process is likely to happen in the model 3L4, given that the final simulation time is significantly greater than the diffusive time-scale over l_{max} . It may start in the model 3L3 for which $t_{\text{final}} \sim \tau_{\text{diff}}(l_{\text{max}})$.

We cannot exclude that the modification of the temperature gradient is in part a transient effect in non-thermally relaxed simulations. The initial conditions for the simulations are based on 1D stellar structures relying on the MLT to describe the transport of heat in the convective core. A readjustment of the structure inducing a change of the location of the Schwarzschild boundary in the 2D simulations cannot be excluded, given the uncertainty inherent to the MLT. But the only process that can readjust the location of the convective boundary over present simulation times is the penetration of convective motions across the convective boundary. A possible readjustment of the structure is thus also part of the process that we aim at characterizing in this work (see discussion in Section 7).

6 APPLICATION TO 1D STELLAR EVOLUTION MODELS AND OBSERVATIONS

6.1 Spectroscopic Hertzsprung–Russell diagram

We implement the scaling relationship for the overshooting distance predicted by present simulations in stellar evolution models and compare these models to observations. For this purpose, the catalogue of data of Castro et al. (2014) is relevant as it covers a large part of the stellar mass range investigated. This observational work provides the position of massive stars of spectral type OB in the Milky Way in the so-called spectroscopic HRD (sHRD). The sHRD uses a value $\mathcal{L} = T_{\text{eff}}^4 / g$ in place of the stellar luminosity L , based on spectroscopically determined effective temperature T_{eff} and surface gravity g of the star. The quantity \mathcal{L} has the advantage that it can be calculated from stellar atmosphere analyses and compared to

Table 4. Characteristic thermal diffusion time-scales $\tau_{\text{diff}} = L^2/\kappa_{\text{rad}}$ and advection time-scales $\tau_{\text{adv}} = L/v_{r,\text{rms}}$ (in s) estimated at the core boundary for all models, based on two characteristic length-scales, $L = l_{\text{max}}(f_{\delta T})$ and $L = H_p$, respectively. κ_{rad} (in cm^2s^{-1}) is the thermal diffusivity and $v_{r,\text{rms}}$ (in cm s^{-1}) is the time-averaged rms radial velocity, both estimated at the core boundary. The last two columns provide the ratio $\frac{\tau_{\text{diff}}}{\tau_{\text{adv}}}$ for the two length-scales.

Model	κ_{rad}	$v_{r,\text{rms}}$	$\tau_{\text{diff}}(l_{\text{max}})$	$\tau_{\text{diff}}(H_p)$	$\tau_{\text{adv}}(l_{\text{max}})$	$\tau_{\text{adv}}(H_p)$	$\frac{\tau_{\text{diff}}}{\tau_{\text{adv}}}(l_{\text{max}})$	$\frac{\tau_{\text{diff}}}{\tau_{\text{adv}}}(H_p)$
3L0	10^7	3.2×10^1	2.6×10^{10}	1.7×10^{13}	1.6×10^7	4.1×10^8	1.6×10^3	4.1×10^4
3L1	10^8	7.8×10^2	3.3×10^9	1.7×10^{12}	7.4×10^5	1.7×10^7	4.4×10^3	10^5
3L2	10^9	4.5×10^3	7×10^8	1.7×10^{11}	1.8×10^5	2.9×10^6	3.9×10^3	5.8×10^4
3L3	10^{10}	2.1×10^4	4.8×10^8	1.7×10^{10}	10^5	6.2×10^5	4.8×10^3	2.7×10^4
3L4	10^{11}	7.5×10^4	1.5×10^8	1.7×10^9	5×10^4	1.8×10^5	3×10^3	9.4×10^3
5L0	7×10^7	1.7×10^2	1.7×10^{10}	4.6×10^{12}	6.4×10^6	10^8	2.6×10^3	4.6×10^4
10L0	7.5×10^8	4.2×10^3	1.2×10^{10}	9.7×10^{11}	7×10^5	6.4×10^6	1.7×10^4	1.5×10^5
15L0	2×10^9	8.5×10^3	10^{10}	5.4×10^{11}	5.2×10^5	3.9×10^6	1.9×10^4	1.4×10^5
20L0	4.5×10^9	1.6×10^4	1.4×10^{10}	3×10^{11}	5×10^5	2.3×10^6	2.8×10^4	1.3×10^5

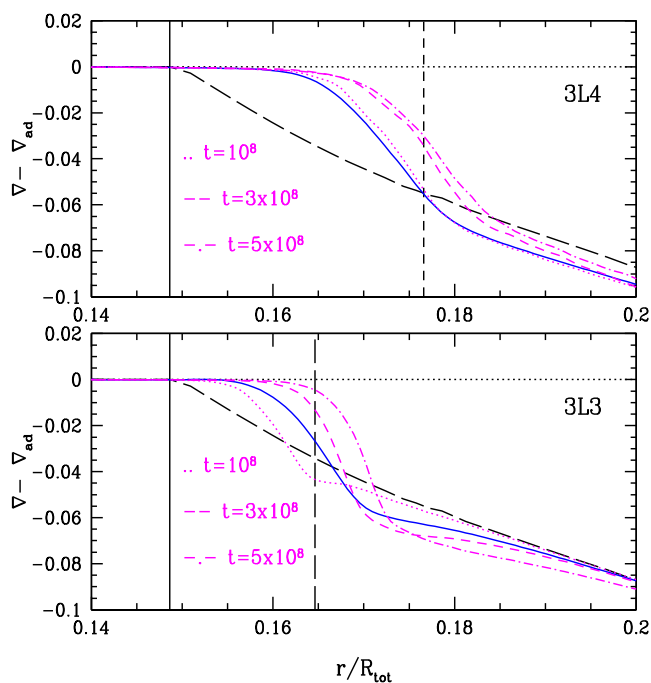


Figure 6. Profile of the time and angular averages of the quantity $(\nabla - \nabla_{\text{ad}})$ in the layers just above the convective core for the most luminous models. The 1D profile of $(\nabla - \nabla_{\text{ad}})$ is indicated by the black solid line and the 1D convective core boundary by the vertical solid line. The location of l_{max} derived from $f_{\delta T}$ is indicated by the vertical dashed line. In both panels, the solid blue line corresponds to the time average between t_{steady} and t_{sim} . The curves in magenta correspond to time averages over $20 \times \tau_{\text{conv}}$ at a given time, as indicated in each panel (time t in s).

stellar evolution models without any knowledge of the distance or the extinction. Castro et al. (2014) derived an empirical location in the sHRD of the ZAMS, for stellar masses above $\sim 9 M_{\odot}$, and terminal-age main sequence (TAMS) that can be directly compared to stellar evolution tracks. Because of the discrepancy in the main-sequence width between observations and models, the main conclusion of their work is that convective core overshooting may be mass dependent and stronger than previously thought for stellar masses $\gtrsim 15 M_{\odot}$. We use this catalogue of data to test the scaling relationship for d_{ov} predicted by present numerical simulations.

Stellar evolution models are calculated using the MESA code (Paxton et al. 2011), which provides the flexibility of easily implementing

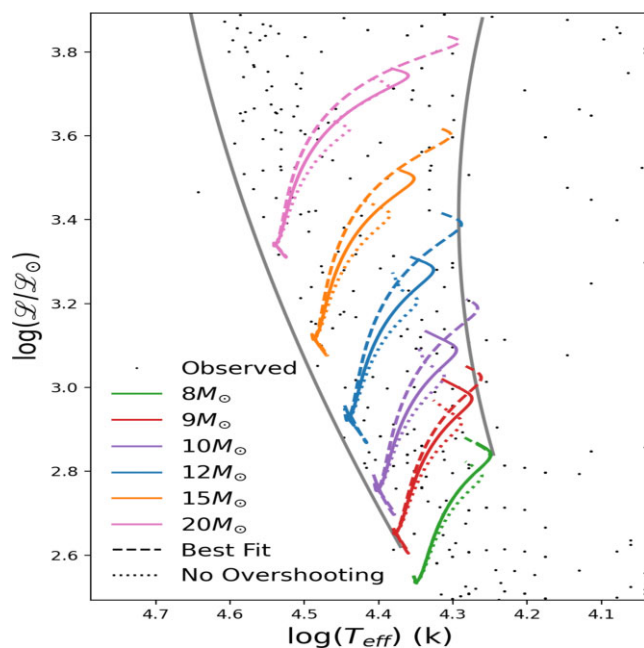


Figure 7. Evolution of massive stars in the sHRD with different treatments of core overshooting. The symbols are observed stars in the Milky Way from Castro et al. (2014). The positions of the ZAMS and the TAMS are indicated by the black solid lines. Coloured solid lines: models evolved with an overshooting law given by equation (14). Dashed lines: models evolved with an arbitrary overshooting length $d_{\text{ov}} = \alpha_{\text{ov}} H_p$ with values of α_{ov} provided in Table 5. Dotted lines: models with no overshooting.

the scaling relation for overshooting distance given by equation (14). Instantaneous mixing is assumed over the distance d_{ov} above the convective core. We have performed calculations adopting either a radiative or an adiabatic temperature gradient in the overshooting layer and find no significant impact on the evolutionary tracks. As done in Castro et al. (2014), we compare the data to solar metallicity models. In Fig. 7, we show the evolution of massive stars in the mass range $8\text{--}20 M_{\odot}$ with no overshooting and with the scaling relationship given by equation (14). The tracks are compared to the Castro et al. (2014) data and to the empirical locations of the ZAMS and the TAMS. Table 5 provides the values of d_{ov}/H_p at the ZAMS and the TAMS, respectively, for the models evolved with the scaling relationship given by equation (14).

Table 5. Values of d_{ov}/H_P for each stellar model evolved with the scaling relationship given by equation (14) at the ZAMS and the TAMS, respectively. α_{ov} is the fitted value for each stellar mass required to roughly reproduce the observed main-sequence width.

M/M_{\odot}	d_{ov}/H_P (ZAMS)	d_{ov}/H_P (TAMS)	Fitted α_{ov}
8	0.09	0.11	0.1
9	0.10	0.13	0.2
10	0.11	0.14	0.3
12	0.13	0.18	0.35
15	0.16	0.23	0.4
20	0.22	0.32	0.45

Table 6. Properties of the binaries used for the comparison with models.

Binary	M/M_{\odot}	T_{eff} (K)	L/L_{\odot}
HD 152218a	19.8 ± 1.5	$33\,400 \pm 1000$	$7.94^{+2.52}_{-1.77} \times 10^4$
HD 152218b	15.0 ± 1.1	$29\,900 \pm 1000$	$4.36^{+1.39}_{-1.48} \times 10^4$
HD 152219a	18.64 ± 0.47	$30\,900 \pm 1000$	$(7.26 \pm 0.97) \times 10^4$
HD 152219b	7.70 ± 0.12	$21\,697 \pm 1000$	$(2.73 \pm 0.51) \times 10^3$
CPD-41°742a	17.8 ± 0.5	$31\,800 \pm 1000$	$5.28^{+0.67}_{-0.68} \times 10^4$
CPD-41°742b	10.0 ± 0.3	$24\,098 \pm 1000$	$5.58^{+0.93}_{-0.94} \times 10^3$

We have also computed models with an arbitrary overshooting length $d_{\text{ov}} = \alpha_{\text{ov}} H_P$ that is fixed for a given stellar mass but increases with mass. The values of α_{ov} for this set of models are chosen to roughly reproduce the main-sequence width and are provided in Table 5. We did not try to reproduce the ZAMS/TAMS empirical positions accurately. This set of models is also shown in Fig. 7. In agreement with the conclusions of Castro et al. (2014), models without overshooting are unable to reproduce the observed main-sequence width. An increasing overshooting distance with increasing stellar mass is required to reproduce the observed width. The overshooting scaling law based on our present hydrodynamical simulations predict this increase with the stellar mass (see Fig. 4). It provides a good fit to the observed main-sequence width for $M \lesssim 10 M_{\odot}$. But it tends to underpredict the value of d_{ov} needed for models of higher mass to reach the observed location of the TAMS. A comparison of the values of d_{ov} given in Table 5 with the fitted values of α_{ov} given in the same table suggests that values predicted by the hydrodynamical simulations are a factor ~ 2 smaller than what is required to reach the observed location of the TAMS.

6.2 Massive binaries

We also test the overshooting scaling law given by equation (14) against a selected sample of massive eccentric binaries, namely HD 152218 (Rauw et al. 2016), HD 152219 (Rosu et al. 2022a), and CPD-41°742 (Rosu et al. 2022b). We limit this analysis to this restricted number of binary systems as they belong to the same young open cluster NGC 6231 and thus have the same metallicity, likely a solar metallicity. In addition, their fundamental properties are inferred using the same methods and tools. This selected sample thus provides a small but homogeneous and consistent set of data to compare to stellar models. Their fundamental properties are provided in Table 6.

Fig. 8 compares evolutionary tracks with different treatments of core overshooting with the observed properties of these binaries. For HD 152218 (Fig. 8, left-hand panel), all models provide a solution within the error bars, but the large error bars do not provide a very stringent test for the treatment of overshooting. For HD

152219 (Fig. 8, middle panel), all models provide a solution to the secondary, while only models with the arbitrary overshooting width from Table 5 provide a solution for the primary. Finally, for CPD-41°742 (Fig. 8, right-hand panel), all models fall within the error bars for the secondary. For the primary, models with the arbitrary overshooting width provide a solution, but the models with the present hydrodynamical relationship provide solutions at the very limit of the error bars. Although this comparison of models with binaries is less conclusive than the one performed with the Castro et al. (2014) data, it suggests that larger overshooting widths than those predicted by the hydrodynamical relationship would provide a better fit, particularly for primaries with masses $\sim 18 M_{\odot}$.

7 DISCUSSION AND CONCLUSION

This work is an initial, exploratory investigation, in which we infer an overshooting width d_{ov} for a broad range of ZAMS stellar models based on hydrodynamical simulations. The present determination of an effective overshooting width, characterizing the extent of mixing on the long-term evolution of the star, is based on an approach relying on extreme events of penetrating flows previously developed for convective envelopes of solar-type stars (e.g. Pratt et al. 2017, 2020; Baraffe et al. 2021). For ZAMS stars, we find that the overshooting distance scales with the stellar luminosity and the convective core radius, resulting in values of d_{ov} that significantly increase with stellar mass. Obtaining this increase is an important achievement, since such an increase is suggested by several observational constraints. But although the results within our framework are qualitatively in agreement with the observed trends, quantitatively, they are unable to match the available data. Indeed, the comparison of stellar evolution tracks to the properties of a sample of Milky Way main-sequence stars suggests that the predicted values of d_{ov} are underestimated for $M \gtrsim 10 M_{\odot}$. The comparison to massive binaries suggests the same limitation. This points to a need for further computational studies, as discussed below.

The diagnostics we have used to examine the present set of 2D simulations have their limitations and several physical or numerical ingredients may increase the values of overshooting lengths. One limitation is our assumption that the overshooting lengths determined within the extreme event framework, which is based on fluxes in an Eulerian approach, characterize the extension of efficient chemical mixing above the convective core. Quantifying the extent of chemical mixing is the prime interest for an application to 1D stellar evolution models. This assumption can be verified with an analysis of mixing based on Lagrangian tracer particles, a direction that will be explored in a future work. The formation of a small nearly adiabatic layer above the convective core of our models due to efficient entropy mixing by the upward penetrating flows indicates that efficient chemical mixing should also proceed between the convective boundary and the location of the maximal overshooting length l_{max} . But the size of the layer for efficient chemical mixing and the one of the nearly adiabatic layer are not expected to be the same, even if the same initial process drives thermal and chemical mixing (i.e. advection by upward flows). Our results suggest that the extent of the nearly adiabatic layer may be limited by thermal diffusion, as observed for the most luminous models when the simulation time exceeds the typical thermal diffusive time-scale in the overshooting layer. Thermal diffusion will not limit the extent of chemical mixing. Internal waves excited by convective plumes at the core boundary could however contribute to additional chemical mixing and extend the size of the chemical mixing layer beyond l_{max} . This is also under

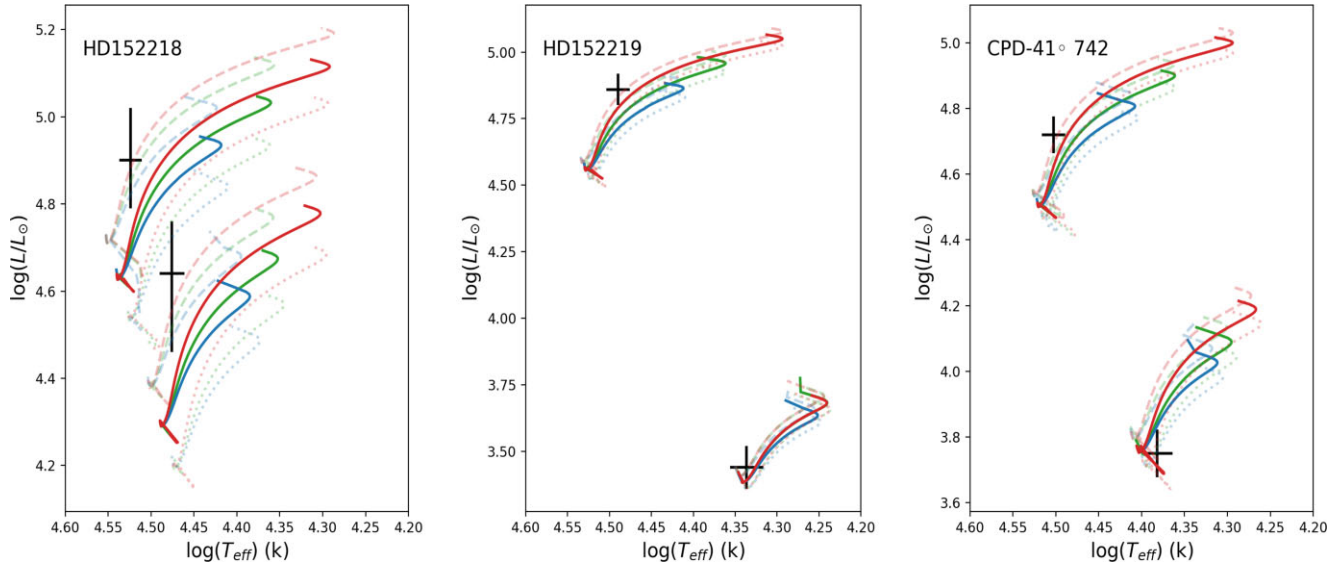


Figure 8. Comparison of evolutionary tracks with different treatments of overshooting and observations for massive binaries in the HRD. Green lines: models evolved with the overshooting law given by equation (14). Red lines: models evolved with an arbitrary overshooting length d_{ov} provided in Table 5 (fitted α_{ov}). Blue lines: models without overshooting. The solid lines correspond to the track for the masses provided in Table 6 and the dashed lines correspond to the tracks for the upper and lower masses within the error bars. Observations are from Rauw et al. (2016) for HD 152218, Rosu et al. (2022a) for HD 152219, and Rosu et al. (2022b) for CPD-41° 742.

further investigation and could provide an interesting process to increase the overshooting lengths derived with present approach.

Extension to 3D geometry is an obvious next step, since the structure and the geometry of penetrating convective flows are expected to be modified in 3D compared to 2D simulations (see Brummell et al. 2002). Despite 2D convective velocities being on average larger than 3D velocities (Meakin & Arnett 2007; Pratt et al. 2020), several works have suggested that the filling factor and the plume geometry could be smaller in 3D than those in 2D (see discussion in Rogers, Glatzmaier & Jones 2006). Simulations in 3D may thus provide larger overshooting lengths, as needed to reproduce stellar observations. But so far no conclusive study of the filling factor and the plume shape using the same simulation framework in 2D and 3D has been performed (see Pratt et al. 2020).

Further numerical studies need to be performed in order to determine the impact of rotation and whether it can provide another driver to increase overshooting lengths and/or to make mixing more efficient (see e.g. Browning, Brun & Toomre 2004). A limitation of the present simulations, and indeed many global simulations of stars, is the fact that they are not thermally relaxed, since this would require simulation times even greater than the values for the thermal diffusion time-scale over a pressure scale height $\tau_{diff}(H_p)$ provided in Table 4. The direct application of the overshooting lengths predicted by these simulations to ‘real’ stars must thus be taken with caution, since the final relaxed state for these simulations may have different properties from present non-thermally relaxed states. This does not however preclude analysing the efficiency of overshooting as a function of stellar mass and luminosity during the slowly evolving transient phase during which convection is considered to be in steady state. One can speculate that even if the convective boundary moves with respect to the initial 1D Schwarzschild boundary after thermal relaxation, the overshooting lengths determined on a dynamical steady state from this new boundary may still be close to the ones determined in this work. Unfortunately, to verify this implies running the simulations over a thermal time-scale, which is computationally

not feasible. More extreme enhancement factors for the luminosity could allow reaching thermal relaxation. But as shown recently for convective envelopes in Baraffe et al. (2021), large enhancement factors can push the simulated conditions away from the original target star, inducing a significant drift from the initial stellar structure.

In addition, the scaling presented in this work is derived for ZAMS stars and may not apply to cores that have evolved on the main sequence. Indeed, the development of a molecular weight gradient at the core boundary due to hydrogen burning will most likely limit the radial penetration of upward flows above the convective core boundary. Numerical simulations of the convective core of main-sequence 5 and 20 M_{\odot} star models indicate much smaller values of l_{max} compared to their ZAMS counterpart (Morison et al., in preparation). In addition, they show no sign of entrainment that could result in an increase of the size of the convective core. Whether 3D, rotation, and/or other instabilities can solve the problem of ‘impenetrability’ of convective flows due to the building of a molecular weight gradient during the evolution on the main sequence is an open question. Other effects and/or improvement of present 2D simulations are needed to increase the overshooting lengths for both ZAMS and main-sequence models.

In conclusion, this work provides results that qualitatively validate the increase of overshooting lengths with stellar mass (or stellar luminosity) suggested by observations (e.g. Castro et al. 2014). Quantitatively, however, the predicted values are underestimated for stellar masses $\gtrsim 10 M_{\odot}$. Our present results apply only to stellar models on the ZAMS. Our study illustrates the challenges and the promise of hydrodynamical simulations. It sets the stage for broader, and more physically detailed, studies to resolve in the future this quantitative discrepancy with observations.

ACKNOWLEDGEMENTS

This work was supported by the ERC grant no. 787361-COBOM and the consolidated STFC grant ST/R000395/1. We are grateful to Noberto Castro for providing data in a user-friendly form and for

useful advices for using the catalogue. We thank our anonymous referee for very valuable comments and suggestions. The authors would like to acknowledge the use of the University of Exeter High-Performance Computing (HPC) facility ISCA and the DiRAC Data Intensive service at Leicester, operated by the University of Leicester IT Services, which forms part of the STFC DiRAC HPC Facility. The equipment was funded by BEIS capital funding via STFC capital grants ST/K000373/1 and ST/R002363/1 and STFC DiRAC Operations grant ST/R001014/1. DiRAC is part of the National e-Infrastructure. Part of this work was performed under the auspices of the U.S. Department of Energy by Lawrence Livermore National Laboratory under contract DE-AC52-07NA27344.

DATA AVAILABILITY

The 1D initial structures are available on the repository: http://pers.o.ens-lyon.fr/isabelle.baraffe/2Dcore_overshooting_2023. The other data underlying this article will be shared on reasonable request to the corresponding author.

REFERENCES

- Anders E. H., Jermyn A. S., Lecoanet D., Brown B. P., 2022, *ApJ*, 926, 169
 Andr assy R., Spruit H. C., 2013, *A&A*, 559, A122
 Andrassy R., Herwig F., Woodward P., Ritter C., 2020, *MNRAS*, 491, 972
 Arnett W. D., Meakin C., 2011, *ApJ*, 733, 78
 Baraffe I., El Eid M. F., 1991, *A&A*, 245, 548
 Baraffe I., Chabrier G., Allard F., Hauschildt P. H., 1998, *A&A*, 337, 403
 Baraffe I., Pratt J., Vlaykov D. G., Guillet T., Goffrey T., Le Saux A., Constantino T., 2021, *A&A*, 654, A126
 Biermann L., 1932, *Z. Astrophys.*, 5, 117
 Bossini D. et al., 2015, *MNRAS*, 453, 2290
 Browning M. K., Brun A. S., Toomre J., 2004, *ApJ*, 601, 512
 Brummell N. H., Clune T. L., Toomre J., 2002, *ApJ*, 570, 825
 Castro N., Fossati L., Langer N., Sim on-D az S., Schneider F. R. N., Izzard R. G., 2014, *A&A*, 570, L13
 Claret A., Torres G., 2016, *A&A*, 592, A15
 Claret A., Torres G., 2019, *ApJ*, 876, 134
 Cristini A., Hirschi R., Meakin C., Arnett D., Georgy C., Walkington I., 2019, *MNRAS*, 484, 4645
 Edelmann P. V. F., Ratnasingam R. P., Pedersen M. G., Bowman D. M., Pratt V., Rogers T. M., 2019, *ApJ*, 876, 4
 Fernando H. J. S., 1991, *Annu. Rev. Fluid Mech.*, 23, 455
 Freytag B., Ludwig H. G., Steffen M., 1996, *A&A*, 313, 497
 Gilet C., Almgren A. S., Bell J. B., Nonaka A., Woosley S. E., Zingale M., 2013, *ApJ*, 773, 137
 Goffrey T. et al., 2017, *A&A*, 600, A7
 Goldreich P., Kumar P., 1990, *ApJ*, 363, 694
 Higl J., M uller E., Weiss A., 2021, *A&A*, 646, A133
 Horst L., Edelmann P. V. F., Andr assy R., R opke F. K., Bowman D. M., Aerts C., Ratnasingam R. P., 2020, *A&A*, 641, A18
 Hotta H., 2017, *ApJ*, 843, 52
 Iglesias C. A., Rogers F. J., 1996, *ApJ*, 464, 943
 Johnston C., 2021, *A&A*, 655, A29
 Jones S., Andrassy R., Sandalski S., Davis A., Woodward P., Herwig F., 2017, *MNRAS*, 465, 2991
 K apyl a P. J., 2019, *A&A*, 631, A122
 Lecoanet D., Quataert E., 2013, *MNRAS*, 430, 2363
 Meakin C. A., Arnett D., 2007, *ApJ*, 667, 448
 Michielsen M., Pedersen M. G., Augustson K. C., Mathis S., Aerts C., 2019, *A&A*, 628, A76
 Montalb an J., Schatzman E., 2000, *A&A*, 354, 943
 Paxton B., Bildsten L., Dotter A., Herwig F., Lesaffre P., Timmes F., 2011, *ApJS*, 192, 3
 Pin on C., Belkacem K., Goupil M. J., 2016, *A&A*, 588, A122
 Pratt J. et al., 2016, *A&A*, 593, A121
 Pratt J., Baraffe I., Goffrey T., Constantino T., Viallet M., Popov M. V., Walder R., Folini D., 2017, *A&A*, 604, A125
 Pratt J., Baraffe I., Goffrey T., Geroux C., Constantino T., Folini D., Walder R., 2020, *A&A*, 638, A15
 Press W. H., 1981, *ApJ*, 245, 286
 Rauw G., Rosu S., Noels A., Mahy L., Schmitt J. H. M. M., Godart M., Dupret M. A., Gosset E., 2016, *A&A*, 594, A33
 Rieutord M., Zahn J. P., 1995, *A&A*, 296, 127
 Rogers F. J., Nayfonov A., 2002, *ApJ*, 576, 1064
 Rogers T. M., Glatzmaier G. A., Jones C. A., 2006, *ApJ*, 653, 765
 Rogers T. M., Lin D. N. C., McElwaine J. N., Lau H. H. B., 2013, *ApJ*, 772, 21
 Rosenfield P. et al., 2017, *ApJ*, 841, 69
 Rosu S., Rauw G., Farnir M., Dupret M. A., Noels A., 2022a, *A&A*, 660, A120
 Rosu S., Rauw G., Naz e Y., Gosset E., Sterken C., 2022b, *A&A*, 664, A98
 Schatzman E., 1993, *A&A*, 279, 431
 Scott L. J. A., Hirschi R., Georgy C., Arnett W. D., Meakin C., Kaiser E. A., Ekstr om S., Yusof N., 2021, *MNRAS*, 503, 4208
 Shaviv G., Salpeter E. E., 1973, *ApJ*, 184, 191
 Stancliffe R. J., Fossati L., Passy J. C., Schneider F. R. N., 2016, *A&A*, 586, A119
 Staritsin E. I., 2013, *Astron. Rep.*, 57, 380
 Strang E. J., Fernando H. J. S., 2001, *J. Fluid Mech.*, 428, 349
 Viallet M., Baraffe I., Walder R., 2011, *A&A*, 531, A86
 Viallet M., Goffrey T., Baraffe I., Folini D., Geroux C., Popov M. V., Pratt J., Walder R., 2016, *A&A*, 586, A153
 Vlaykov D. G., Baraffe I., Constantino T., Goffrey T., Guillet T., Le Saux A., Morison A., Pratt J., 2022, *MNRAS*, 514, 715
 Zahn J. P., 1991, *A&A*, 252, 179
 Zahn J. P., 1992, *A&A*, 265, 115

This paper has been typeset from a $\text{\TeX}/\text{\LaTeX}$ file prepared by the author.